

# Evaluation of Rheological and Thermal Behavior of Ceramic Materials during Liquid Phase Sintering with Numerical-Experimental Procedure

E. Salahi<sup>\*1</sup>, H. Yaghoubi<sup>1</sup>, F. Taati<sup>2</sup>

<sup>1</sup>Ceramic Science and Engineering Department, Material and Energy Research Center (MERC), Meshkin dasht, Karaj, Tehran, Iran.

<sup>2</sup>Applied Physics and Mathematics Department, Material and Energy Research Center (MERC), Meshkin dasht, Karaj, Tehran, Iran.

received March 19, 2017; received in revised form July 10, 2017; accepted July 18, 2017

## Abstract

Its shear and bulk viscosity, as well as dynamic viscosity, describe the rheological behavior of a ceramic body during liquid-phase sintering. The thermal behavior of a ceramic body during sintering, including viscous flow deformation, anisotropic shrinkage, heterogeneous densification, has a significant influence on both the final body's dimensional precision and the densification process. In this paper, the numerical-experimental method was developed to study both the rheological and thermal behavior of hard porcelain ceramic body during the liquid phase sintering process. After analysis of the raw materials, a standard hard porcelain mixture was designed and prepared as a ceramic body. The finite element method in the CREEP user subroutine code in ABAQUS was implemented for the ceramic specimens during the liquid-phase sintering process. Densification results confirmed that the bulk viscosity was well-defined with relative density. Also, deflection and shrinkage outputs proved that the shear viscosity was well-defined with dynamic viscosity. The sintering stress exceeded the hydrostatic stress during the entire sintering time so the sintering process occurred completely. Dilatometry, SEM, XRD investigations as well as simulation results for bulk viscosity confirmed the “mullitization plateau” as very limited expansion during the final sintering stage.

*Keywords:* Rheological behavior, hard porcelain, liquid phase sintering, numerical-experimental analysis

## I. Introduction

One of the most important stages in ceramic manufacturing is the sintering process. During this stage, a ceramic part undergoes thermo-mechanical loading, which leads to shape deformation of the sintered body. Not only do deformation, deflection, and cracks occur, non-uniform shrinkage takes place in the sintered bodies<sup>1–5</sup>. The loss of a product's final shape can be defined as the pyroplastic or viscous flow deformation, which takes place more frequently in highly vitrified ceramic bodies such as porcelain<sup>2–4</sup>. This loss in dimensional precision and deformation during the sintering process lead to an increase in cost of producing the ceramic body, especially if the sintered ceramic body then needs machining or finishing<sup>3–5</sup>. Therefore, prediction and modification of the distortion in a ceramic body during sintering has attracted many researchers and producers to develop models to describe the sintering process, but the road to the commercial benefits is still too far<sup>4–7</sup>. The non-economical trial and error method is routinely carried out to predict and modify the final dimensions and obtain the desired ceramic parts after sintering. The finite element method (FEM) is an alterna-

tive cost-benefitted procedure to predict the shape instabilities during the sintering process<sup>3–7</sup>. Therefore, understanding the rheological and thermal behavior of green ceramic compacts during liquid phase sintering is essential.

The rheological behavior is defined as the resistance against viscous flow deformation and shrinkage<sup>1–4</sup>. Although it is a function of the physical and thermo-mechanical properties of the material, e.g. relative density, temperature, grain size, diffusion coefficient, and activation energy, it can be parameterized mainly by the shear, bulk, and dynamic viscosities. Considerable conceptual and experimental difficulties are involved in determining the rheological parameters in ceramic materials during the liquid phase sintering process<sup>1–8</sup>; however, different methods and models for determining these parameters have been proposed in the literature<sup>5</sup>. The shear viscosity ( $G_p$ ) can be expressed in a form very similar to the bulk viscosity ( $K_p$ ) and then approximated by assuming  $\frac{G_p}{K_p} = 0.6$  just before liquid formation, as suggested by Riedel *et al.*<sup>6–8</sup>. Moreover, the uniaxial dynamic viscosity can be determined in the creep test<sup>4–7</sup>. Another approach proposed in the literature is that, at low stresses (about 1 Mpa), the green ceramic body undergoing densification can be treated as a linear viscous material<sup>4, 10–11</sup>. So, to

<sup>\*</sup> Corresponding author: [kesalahi@yahoo.com](mailto:kesalahi@yahoo.com)

overcome these problems, an alternative is finite element simulation supported by some economical experimental tests<sup>2–9</sup>.

Other efforts have been devoted to the development of the theory of sintering to predict the final density and dimensions. However, the major challenges here are, (i) how to predict both the anisotropic shrinkage and heterogeneous densification, (ii) how to take the simultaneous effect of gravity and friction force into account, and (iii) how to measure the sintering and hydrostatic stress through the ceramic body during the liquid phase sintering process<sup>1–7</sup>. These challenges define the thermal behavior of a ceramic body during liquid phase sintering. Determining these key parameters is essential for ceramic manufacturers to estimate the densification process and final shape of a ceramic body.

The major objective of this paper is to develop a numerical-experimental method to study both the rheological and thermal behavior of hard porcelain ceramic body during liquid phase sintering. For this purpose, the continuum model is used based on the sintering kinetics of a porous nonlinear-viscous material. This macroscopic model is implemented using ABAQUS with the CREEP subroutine. The shape distortion, viscous flow deformation, anisotropic shrinkage and heterogeneous density of hard porcelain body have been addressed. The other novelties of this paper are to accurately determine (i) the dynamic viscosity, (ii) relative density distribution, and (iii) deformation evolution as a function of sintering time.

The present study is organized as follows: Section 2 presents the sintering model and the constitutive law including initial and boundary conditions. Section 3 describes the numerical procedure to implement the model with the CREEP subroutine in ABAQUS. Section 4 includes the experimental procedures for preparing hard porcelain samples in different geometries to obtain enough data to select a proper model for dynamic viscosity as well as to calibrate and validate the numerical model. Section 5 presents a comprehensive comparison between the experimental and simulation results.

## II. Sintering Model

### (1) Constitutive law

The macroscopic approach to modeling the sintering process with the aid of continuum mechanics has been developed by V.V. Skorohod. Further investigations have been carried out by E. A. Olevsky<sup>16–18</sup>. The model proposes a constitutive law for a porous green body with a two-phase material which includes a porous body skeleton phase and a void one. The skeleton is assumed to be made up of individual particles having a general linear-viscous incompressible isotropic behavior, and the distribution of the voids is isotropic. Therefore, the overall response is assumed to be isotropic. The constitutive model described in this paper follows the formulation of the continuum theory for sintering of porous viscous materials<sup>12–24</sup>. The Skorohod-Olevsky Viscous Sintering (SOVS) constitutive relationship for a linear viscous porous material is presented as,<sup>24–27</sup>

$$\dot{\epsilon}_{ij}^{in} = \frac{\dot{\sigma}_{ij}}{2G_p} + \frac{(\sigma_m - \sigma_s)}{3K_p} \delta_{ij} \quad (1)$$

where,  $\dot{\sigma}_{ij}$  and  $\sigma_m$  are the deviatoric and hydrostatic parts of the true stress tensor  $\sigma_{ij}$ ,  $\delta_{ij}$  is the Kronecker delta,  $\sigma_s$  is the sintering stress, which will be elaborated later,  $G_p$  and  $K_p$  are the effective shear and bulk viscosity of the ceramic body, which are defined in the following<sup>16–24</sup>,

$$G_p = (1-\theta)^2 \eta \quad (2)$$

$$K_p = \frac{4(1-\theta)^3}{3\theta} \eta \quad (3)$$

Here  $\eta$  is dynamic viscosity of the ceramic material. It is a temperature-dependent property that should be defined correctly to obtain a finite element model with reasonably accurate prediction capability. The experimental method in the later section is designed to find such an accurate model for the dynamic viscosity function for ceramic materials during liquid phase sintering.

As mentioned above,  $\sigma_s$  is the sintering stress or the Laplace pressure. It is the driving force for densification due to interfacial energy of pores and grain boundaries. This stress caused by surface tension acting on the pore surface perpendicularly is calculated as,

$$\sigma_s = \frac{3\gamma}{r_0} (1-\theta)^2 \quad (4)$$

where  $\gamma$  is the material surface tension,  $r_0$  is the initial particle radius and  $\theta$  is relative porosity<sup>24–28</sup>.

The total strain in the sintering body including elastic and inelastic strain is given as<sup>24</sup>,

$$\epsilon_{kl}^{tot} = \epsilon_{kl}^{el} + \epsilon_{kl}^{in} \quad (5)$$

The elastic part of the material response is assumed to be isotropic and characterized by Hooke's Law as Eq. (6)<sup>24–27</sup>. It is noted that the elastic modulus of the ceramic body depends on the relative density according to Eq. (7)<sup>15–17, 27–28</sup>.

$$\dot{\sigma}_{ij} = C_{ijkl} \dot{\epsilon}_{kl}^{el} \quad (6)$$

$$E = E_0 \exp(-b_0(1-\rho)) \quad (7)$$

in which  $E_0$  is the elastic modulus of a fully dense material and  $b_0$  is the material constant,  $C_{ijkl}$  is the elastic stiffness matrix and  $\dot{\epsilon}_{kl}^{el}$  is the elastic strain rate.

Differentiating Eq. (5) with respect to time and combining with Eq. (6) gives the overall constitutive behavior as<sup>24</sup>,

$$\dot{\sigma}_{ij} = C_{ijkl} (\dot{\epsilon}_{kl}^{tot} - \dot{\epsilon}_{kl}^{in}) \quad (8)$$

the inelastic strain rate tensor ( $\dot{\epsilon}_{kl}^{in}$ ) that is formulated in Eq. (1).

### (2) Conservation equations, boundary and initial conditions

The other governing equations for modeling the sintering process based on the continuum mechanics are mass and momentum conservation which are given as<sup>16</sup>,

$$\frac{\dot{\rho}}{\rho} = -\epsilon_{kk} \quad (9)$$

$$\sigma_{ij,j} + f_i = 0 \quad (10)$$

in which,  $\dot{\rho}$  is the time derivative of relative density ( $\rho$ ),  $\epsilon_{kk}$  is the first invariant of the strain rate,  $\sigma_{ij}$  is the true stress and  $f_i$  is the body force<sup>16</sup>.

The initial relative density and particle size was measured at about 0.694 and 3.9  $\mu\text{m}$ , respectively. The friction effect between the specimens with refractory supports was also measured based on the Coulomb friction law with an isotropic friction coefficient equal to 0.2. The gravity was also considered  $9.81 \left(\frac{\text{m}}{\text{s}^2}\right)$ .

### III. Numerical Simulation

#### (1) Implementation of the finite element method

The finite element method (FEM) with C3D8I mesh (8-node linear brick, incompatible element), iterative method for equation solver and explicit/implicit integration method are used for simulation of the sintering process in ABAQUS with the user subroutine CREEP. Generally, the user subroutines are provided to increase the functionality of several ABAQUS capabilities for which the usual data input methods alone may be too restrictive. The CREEP user subroutine provides an extremely powerful and flexible analyzing tool for time-dependent volumetric shrinkage viscoplastic behavior of materials. This user subroutine has been written as FORTRAN code and included in a model when the finite element analysis has been executed by ABAQUS<sup>29</sup>. The logarithmic strain is used for geometrically nonlinear analysis. The relative density can be described as,

$$\rho = \rho_0 \exp(-\epsilon_{kk}) \quad (11)$$

where  $\rho_0$  and  $\rho$  are the initial and final relative density, respectively. The volume strain  $\epsilon_{kk}$  is equal to the swelling strain in a 3D sample, as shown in Eq. (12)<sup>12–13</sup>.

$$\epsilon_{kk} = \epsilon_{xx} + \epsilon_{yy} + \epsilon_{zz} \quad (12)$$

The incremental creep is calculated as follows<sup>12–13, 24</sup>,

$$\Delta \epsilon^{\text{cr}} = \frac{1}{3} \Delta \bar{\epsilon}^{\text{sw}} \mathbf{I} + \Delta \bar{\epsilon}^{\text{cr}} \mathbf{n} \quad (13)$$

where  $\Delta \bar{\epsilon}^{\text{cr}}$  and  $\Delta \bar{\epsilon}^{\text{sw}}$  are the equivalent creep strain and the incremental volumetric swelling strain, respectively.  $\mathbf{n}$  is the direction normal to the yield surface, given as follows<sup>17–18, 30–31</sup>,

$$\mathbf{n} = \frac{\partial \sigma_e}{\partial \bar{\sigma}} = \frac{3\bar{\sigma}}{2\bar{q}} \quad (14)$$

here  $\bar{\sigma}$  is the deviatoric stress and  $\bar{q}$  is the von Mises equivalent deviatoric stress. From Eq. (1), the incremental form of the creep strain can be expressed as,

$$\Delta \epsilon^{\text{cr}} = \frac{\text{tr}(\bar{\sigma}) \Delta t - 3\bar{\sigma}_s \Delta t}{9K_p} \mathbf{I} + \frac{\bar{\sigma} \Delta t}{2G_p} \quad (15)$$

Comparison between Eq. (13) and Eq. (15) leads to the following relations:

$$\frac{\text{tr}(\bar{\sigma}) \Delta t - 3\bar{\sigma}_s \Delta t}{9K_p} \mathbf{I} = \frac{1}{3} \Delta \bar{\epsilon}^{\text{sw}} \mathbf{I} \quad (16)$$

$$\frac{\bar{\sigma} \Delta t}{2G_p} = \Delta \bar{\epsilon}^{\text{cr}} \mathbf{n} = \Delta \bar{\epsilon}^{\text{cr}} \frac{3\bar{\sigma}}{2\bar{q}} \quad (17)$$

and hence the incremental creep strain components can be obtained as follows<sup>17–18, 30</sup>,

$$\Delta \bar{\epsilon}^{\text{sw}} = \frac{\text{tr}(\bar{\sigma}) - 3\bar{\sigma}_s}{3K_p} \Delta t = -\frac{P + \bar{\sigma}_s}{K_p} \Delta t \quad (18)$$

$$\Delta \bar{\epsilon}^{\text{cr}} = \frac{\bar{q}}{3G_p} \Delta t \quad (19)$$

in which  $P = -\frac{1}{3} \text{tr}(\bar{\sigma})$  is the equivalent pressure stress (hydrostatic pressure)<sup>17–18</sup>.

From ceramic engineering, the shrinkage anisotropy has a significant influence on final dimensional precision of a ceramic body. Therefore, to determine the shrinkage anisotropy, the factor  $K_{xy}$  is defined as,

$$K_{xy} = 100 \left( 1 - \frac{\epsilon_{xx}}{\epsilon_{yy}} \right) \quad (20)$$

where  $\epsilon_{xx}$  is the logarithmic strain or shrinkage in the plane of the casting direction and  $\epsilon_{yy}$  the same in the transverse direction.

The fraction of frictional work converted to heat was neglected in this work, because of the low weight of sample, low friction coefficient, thermal equilibrium in the small box electrical furnace and low contact area between sample and refractory holder; however, the frictional force between sample and substrate and gravitational force influence was included in the simulation.

Finally, it should be mentioned that the curve fitting, parameter estimation, and error analysis were performed with Wolfram Mathematica 8.0 Software.

### IV. Experimental Procedure

In this section, the experimental procedure for determining the thermal properties of the hard porcelain bodies is explained. Experimental tests measuring the shrinkage behavior of specimens along different directions, tensile strength, water absorption, bulk density, permanent linear change (PLC), microstructure evaluation, phase analysis, and dilatometry were performed.

This ceramic body is formulated based on quartz, feldspar, and clay. Hence, its pyroplastic deformation is mainly affected by its mineral and chemical compositions<sup>12</sup>. Therefore, as the first step in the procedure, both of these have to be analyzed. For the mineral aspect, the phases of its raw materials were analyzed by means of X-ray diffraction (XRD) and the results are shown in Fig. 1. The chemical composition of the formulated body determined by means of X-ray fluorescence (XRF) (PANalytical Minipal 4) is presented in Table 1.

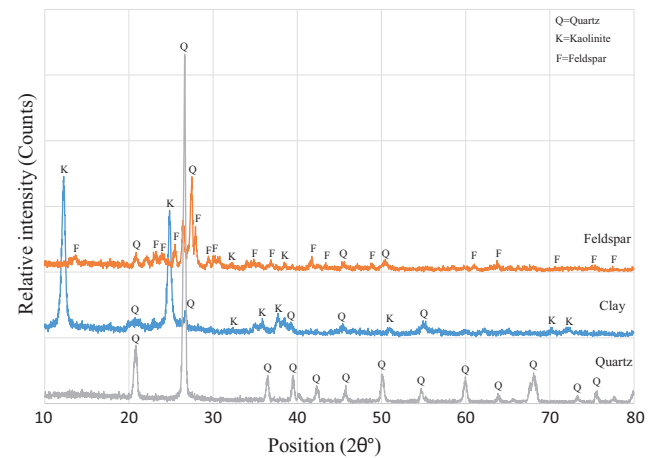


Fig. 1: XRD patterns of the raw materials.

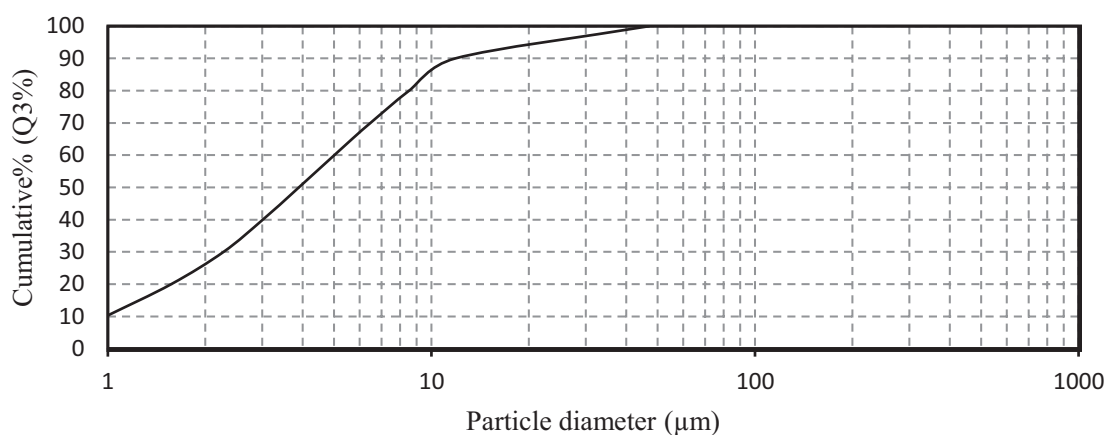
After raw material analysis, the next step is to prepare the final ceramic slip. This step consists of two stages. First, all the non-plastic raw materials, such as feldspar and quartz and some parts of plastic materials, such as clay,

were milled for 20 h in a laboratory ball mill. This suspension was then mixed with the leftover clay in the laboratory mixer. During this procedure, the solid concentration was held constant at 66 % weight. The density of the slip, determined with a pycnometer, was also held at 1690 g/l. The Ford cup/ASTM Number 2 was used to determine the slip viscosity. It was about 85 s. The distribution of particle size in the slip obtained with a laser particle size analyzer (Fritsch Particle Sizer 'analysette 22') is presented in Fig. 2. It indicates that  $d_{10}=0.98$ ,  $d_{50}=3.89$ ,  $d_{90}=11.84$   $\mu\text{m}$ .

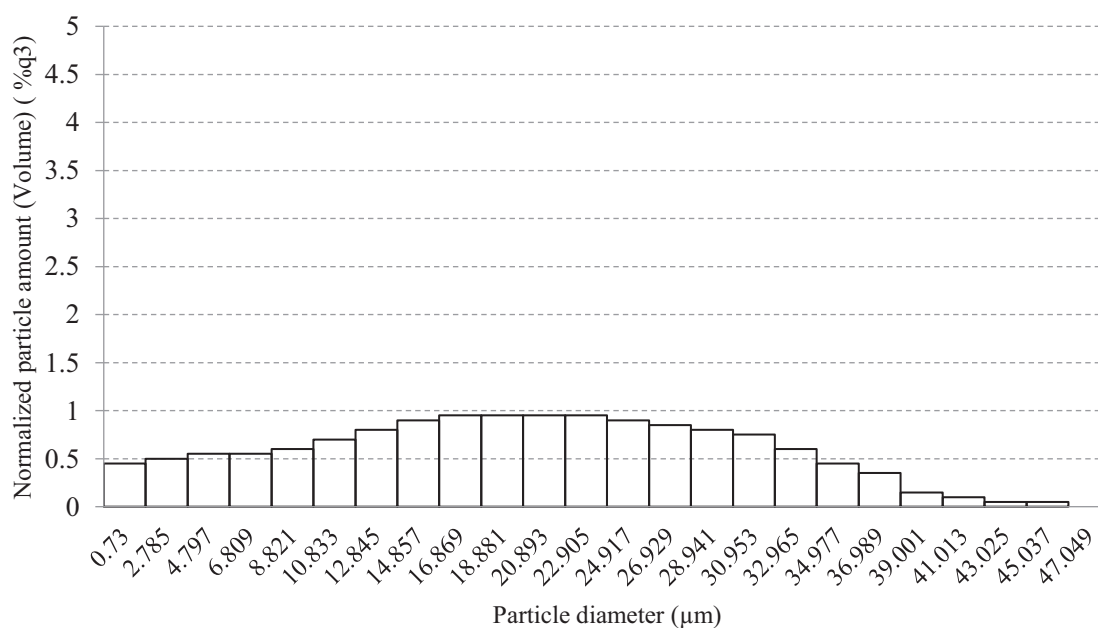
Several samples were prepared from the slip. The samples were shaped by means of two methods: slip casting in a plaster of Paris mold and uniaxial pressing of granules in a steel mold. The dimensions of the rectangular samples were  $5.8 \times 36 \times 260$  mm. The pressed samples had dimensions of  $103 \times 22$  mm with different thicknesses (6, 9.5 and 16.5 mm). The uniaxial pressure of the press was about 25 bar. The spherical granules were formed in a laboratory spray dryer from the same slip-casting suspension. The mean size and relative humidity of the granules was about 210  $\mu\text{m}$  and 2 %, respectively.

**Table 1:** Chemical composition of hard porcelain body.

Chemical compound	MgO	CaO	K <sub>2</sub> O	Na <sub>2</sub> O	TiO <sub>2</sub>	Fe <sub>2</sub> O <sub>3</sub>	Al <sub>2</sub> O <sub>3</sub>	SiO <sub>2</sub>	L.O.I
Weight%	0.5	0.67	1.77	0.33	0.05	0.32	25.7	63.5	7.16



(a)



(b)

**Fig. 2:** Laser particle size distribution of porcelain slip in (a) cumulative distribution and, (b) normalized particle amount format.



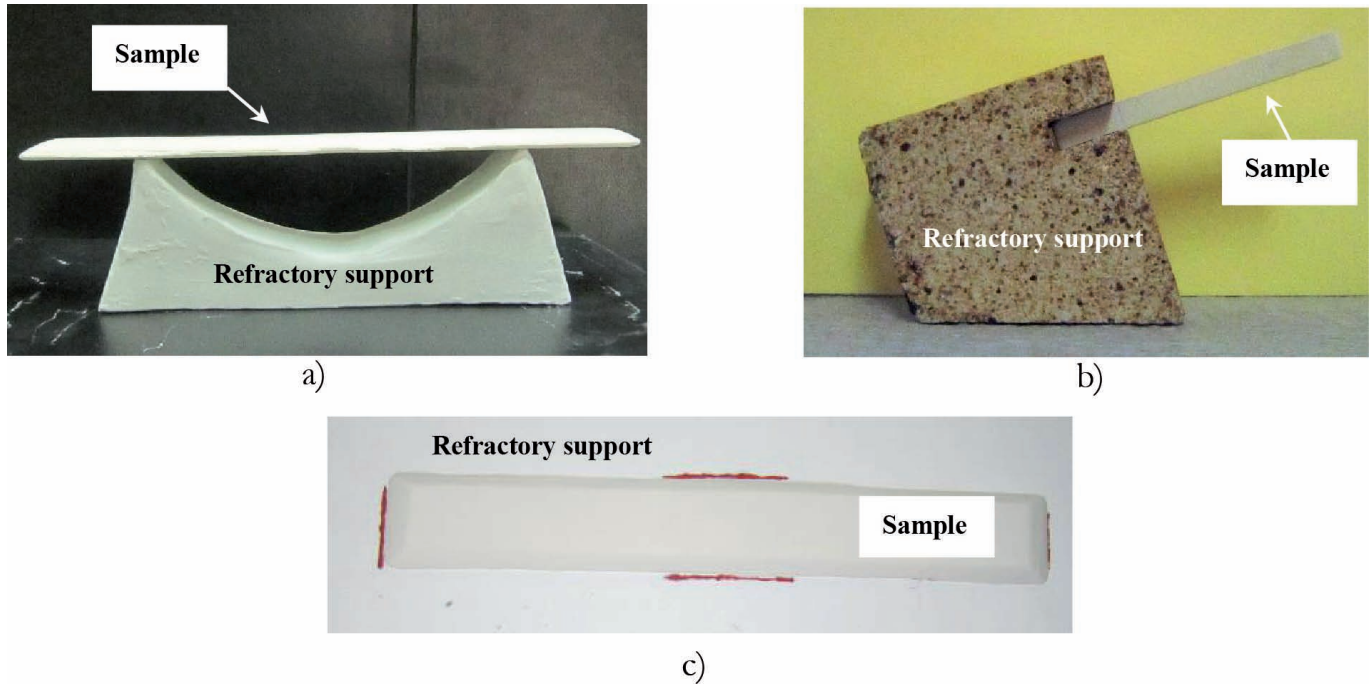


Fig. 3: (a) Midpoint deflection test and (b) sinter-bending test set-up (c) free sintering sample.

To evaluate the sintering model, three different configurations as shown in Fig. 3 were designed. Since both gravitational and frictional force have effects on the deformation, the designed configurations were chosen based on different levels of these effects. The sample in Fig. 3a will experience a maximum frictional and minimum gravitational force, the sample in Fig. 3b will experience a minimum frictional and maximum gravitational force, whilst the sample in Fig. 3c will experience their combinatorial effect. All the samples were placed on refractory supports. The sample in Fig. 3a, midpoint deflection test, was used to select a proper model for dynamic viscosity and calibrate the FE model for the sintering procedure. The samples in Figs. 3b and 3c, sinter bending and free sintering test, were used to validate the model and simulation.

The samples were sintered according to the isothermal-stage firing curve in Fig. 4. In this sintering process, there are no temperature gradients that could lead to cracking or to distortion formation. The average heating and cooling rate was 5.6 and 1.65 °C/min, respectively. The temperature was increased monotonically to a sintering hold temperature and reduced to room temperature afterward.

Dynamic sintering viscosity ( $\eta$ ) is an important physical property that affects pyroplastic deformation. It is defined as a function of temperature  $T$  [3–9],

$$\eta(T) = \frac{5\rho_b g L(T)^4}{32\dot{\delta}(T)h(T)^2} \quad (21)$$

in which  $\dot{\delta}$  is the time derivative of the total deflection  $\delta$ ,  $h$  is the sample thickness,  $L$  is the distance between the supports,  $\rho_b$  is the bulk density of the body, and  $g$  is the gravitational constant. Temperature is also defined as a function of time according to the firing curve shown in Fig. 4.

Moreover, other important physical properties of the samples are apparent porosity ( $P$ ), bulk density ( $\rho_b$ ). They

are measured according to the ASTM C20–00 (2015) standards as follows,

$$P\% = \frac{W_w - W_d}{W_d} \times 100 \quad (22)$$

$$\rho_b = \frac{W_d}{W_w - W_s} \quad (23)$$

where  $W_w$ ,  $W_d$  and  $W_s$  are the wet weight, dry weight and the weight of sample suspended in the water, respectively. This experimental result is reported in Fig. 10 for comparison with the simulation results.

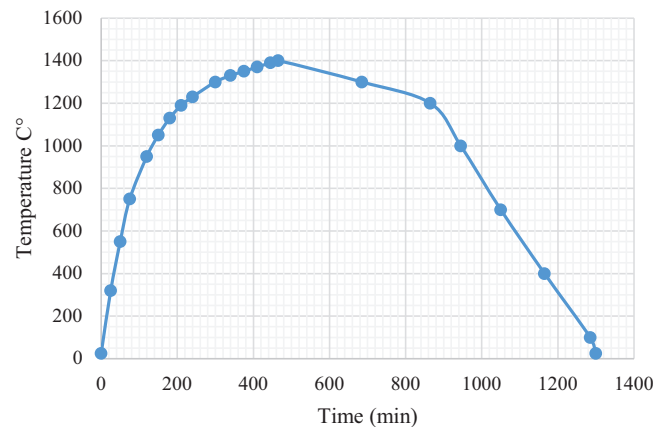


Fig. 4: Designed firing curve in a laboratory electrical furnace.

Because of the significant influence of the microstructure changing on the shear, bulk and dynamic viscosity, the microstructure of both the dried and fired samples was investigated by means of scanning electron microscopy (SEM) in combination with energy-dispersive X-ray (EDX) spectroscopy. The samples were ground and polished in preparation for SEM. The polished surfaces of the samples were chemically etched in aqueous 5 % hydrofluoric acid solution for 10 min. The crystalline phas-

es of samples fired at different temperature were determined using an X-ray diffraction (XRD) with  $\text{CuK}\alpha$  radiation. The scans were recorded in the  $10-90^\circ 2\theta$  range. The dilatometric test was also performed to measure shrinkage during the sintering process from room temperature to  $1400^\circ\text{C}$ . This test result is reported in Fig. 15.

## V. Results and Discussion

In this section, the results of the test experiments and the FE simulation to obtain the pyroplastic deformation, dynamic viscosity and other important physical properties are presented and compared.

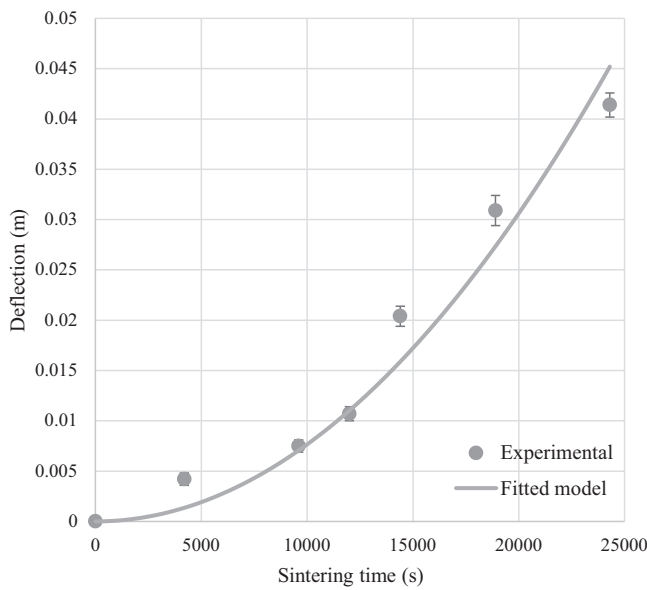


Fig. 5: Fitted model among experimental data for pyroplastic deflection..

One important result is the deflection,  $\delta$ , of the sample during the sintering process. It was obtained by measuring the curvature in the midpoint deflection test and plotted versus sintering time in Fig. 5. Since the time derivative of this deflection,  $\dot{\delta}$ , is an important property, a model should be fitted to the midpoint deflection data and then its time derivative found. For this purpose, let  $\delta_i$  be the deflections measured at time  $t_i$ . The models  $f_j(t, \theta)$ ,  $j = 1, 2, \dots, N$  with parameters  $\theta \in \mathbb{R}^{K_j}$  are  $j$  different competing models selected to fit to the data. The Akaike information criterion (AIC) can be used as a mean of comparison. It is defined as,

$$\text{AIC}_j = n \log(\text{RSS}_j) + 2K_j \quad (24)$$

in which RSS is the Estimated Residual of Fitted Model and is calculated by

$$\text{RSS}_j = \sum_{i=1}^n (\delta_i - f_j(t_i, \theta))^2 \quad (25)$$

This criterion is applied to find the simplest model with the least number of parameters ( $K$ ) that can fit to the data with reasonably good accuracy. This corresponds to the minimum AIC value. This was calculated for five different models presented in Table 2. It indicates that the 4th model has the minimum AIC value, so it is the best one to define the deflection as a function of time. The comparison between this best-fit model and experimental results is shown in Fig. 5.

Having selected 4th model to define deflection as a function of time, one can easily obtain the deflection rate, i.e. its derivative with respect to time can be obtained as,

$$\dot{\delta} = \frac{d\delta}{dt} (\text{m/s}) = 1.53131 \times 10^{-10} t \quad (26)$$

here  $t = 0$  corresponds to  $600^\circ\text{C}$ .

Now, to find a proper model for the dynamic viscosity  $\eta$ , it has been calculated using Eq. (21) at some temperatures and then the best model from the competing models describing available data is selected. To this end, at each temperature, bulk density and thickness were measured, deflection rate  $\dot{\delta}$  was calculated using Eq. (26) and considering the firing curve presented in Fig. 4. These values along with the constant gravitational and span length are substituted into Eq. (21) to obtain the experimental dynamic viscosity, shown by orange disk in Fig. 6. Competing models and their AIC values are listed in Table 3. It can be concluded that Model 5 is the best model to describe the available experimental dynamic viscosity data. The outcome of this model for different temperatures is illustrated in Fig. 6. It indicates an excellent fit between the model's response and the experimental data.

As another measure of accuracy of the models selected above for  $\eta$ , it has been substituted in the FE model and the deflection of the samples during the liquid phase sintering process in the midpoint deflection test have been predicted. The outcome of this simulation is shown in Fig. 7 together with the deformation at the real test samples at different temperatures. They indicate a good accordance of the simulated results with the experimental tests.

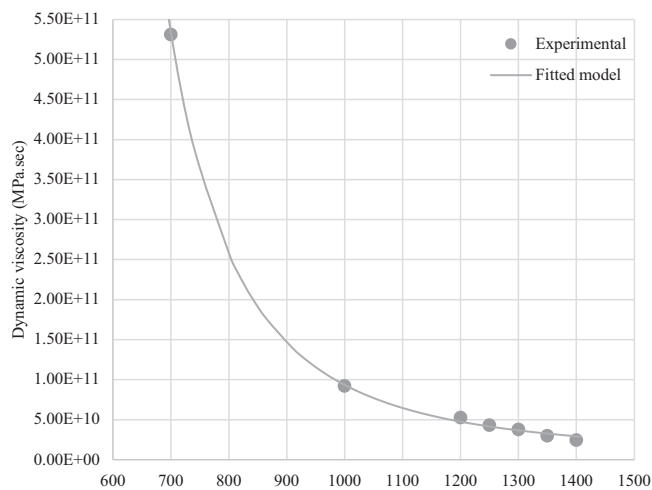
Table 2: Proposed models to find the best fit for pyroplastic deflection.

Model No.	$f(t, \theta)$ Proposed models	K Number of parameters	RSS Estimated residual	AIC
Model 1	$-1.40 \times 10^{-4} + 5.26 \times 10^{-7}t + 5.13 \times 10^{-11}t^2$	3	4.055E-5	-25.69
Model 2	$2.13 \times 10^{-3} + 7.11 \times 10^{-11}t^2$	2	2.98E-5	-26.74
Model 3	$5.05 \times 10^{-7}t + 5.19 \times 10^{-11}t^2$	2	5.6E-5	-27.68
Model 4	$7.66 \times 10^{-11}t^2$	1	2.11E-5	-27.76
Model 5	$1.02 \times 10^{-3} - 5.34 \times 10^{-7}t + 1.69 \times 10^{-10}t^2 - 3.22 \times 10^{-15}t^3$	4	13.8E-5	-24.73

**Table 3:** Proposed models to find the best fit for dynamic viscosity.

Model No.	$f(t, \theta)$ Proposed models	K Number of parameters	AIC
Model 1	$2.158 \times 10^{12} - 3.94206 \times 10^9 T + 1.55648 \times 10^6 T^2$	3	156.859
Model 2	$5.57681 \times 10^{11} - 31.328 T^2$	2	162.966
Model 3	$4.34495 \times 10^{11} - 179.479 T^3$	2	163.763
Model 4	$5.87341 \times 10^{12} - 1.41305 \times 10^{10} T + 1.14597 \times 10^7 T^2 - 3108.82 T^3$	4	147.058
Model 5	$1.61954 \times 10^9 \exp(\frac{4055.11}{T})$	2	140.541

Moreover, Fig. 8 shows the simulation results obtained in [0, 405] min. Comparing these with the real test data reveals a good match between them. This means that the shear viscosity modulus and dynamic viscosity (5<sup>th</sup> model) used in the simulation process are near the real ones<sup>31–33</sup>.

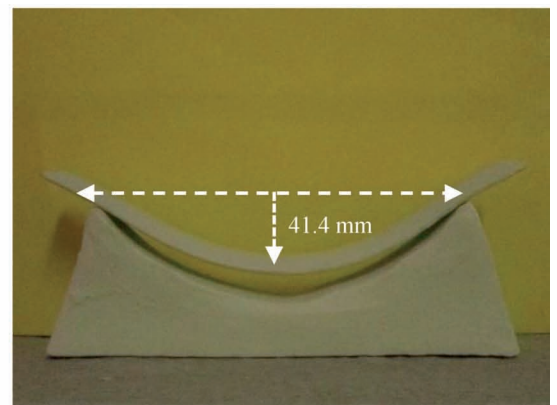
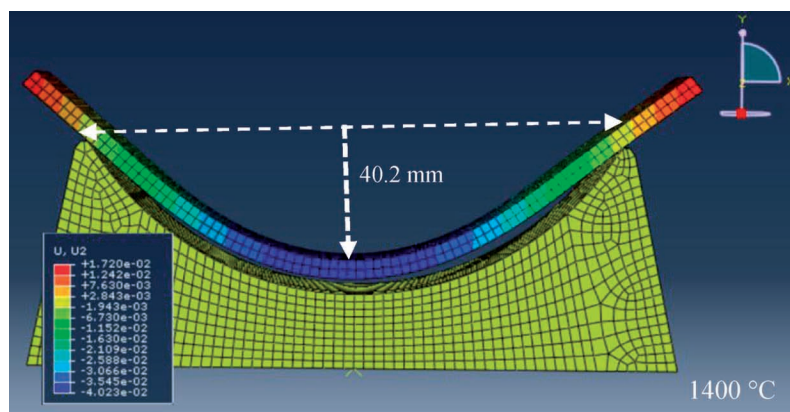
**Fig. 6:** Fitted model among experimental data for dynamic viscosity.

However, there is a slight mismatch between the experimental and simulation results for deflection at  $t = 0$  min and around  $t = 330$  min. For the former, the experimental result shows no deflection, whereas the simulation result exhibits less than 3 mm deflection. This is due to the elastic deflection of the sample stemming from the thermal stress at  $T = 600^\circ\text{C}$ . It was recovered when the sample was extracted from the furnace, and therefore cannot be measured experimentally. The mismatch around 330 min

might be due to instrumental imprecision or inaccurate estimation of effective shear viscosity, at this time.

The simulation result for the linear shrinkage of ceramic body in X, Y and, Z-directions was obtained and compared with the PLC experiment data. The results shown in Fig. 9 reveals the accuracy of the simulation's outcome. From the simulation and experiment results, it was found that the linear shrinkage along the normal axis of slip casting (X-direction) is about 1.15 times larger than that of casting direction, because of preferential orientation of clay platelets. In deflocculated porcelain slip, the clay platelets diffuse toward the surface of the plaster mold and a green ceramic layer is formed over time. As the clay particles approach the wall, they orient with the long dimension parallel to the capillary channel direction because of water shear across the channel. As the channel narrows, the particles wedge into the wall with the orientation geometry, resulting in dense packing with preferential orientation<sup>10–14</sup>.

The next simulation is carried out to investigate the accuracy of the model to predict the evolution of relative density during the sintering time. As shown in Fig. 10, there is a good match between the experimental and simulation results. It should be noted that the abrupt increase in the relative density at the middle step of sintering time ( $t = 5000$  to  $20000$  s) obtained by the experiment has been captured with good accuracy by the proposed model. This phenomenon occurs because of the significant increase in the amount of liquid phase. Furthermore, a decrease in the glassy phase viscosity leads to filling out of the pores, which is confirmed by SEM investigations, and previous findings<sup>3–4, 16, 27</sup>.

**Fig. 7:** Comparison of shape distortion of real sample and finite element simulation after the sintering process for the slip-cast sample.

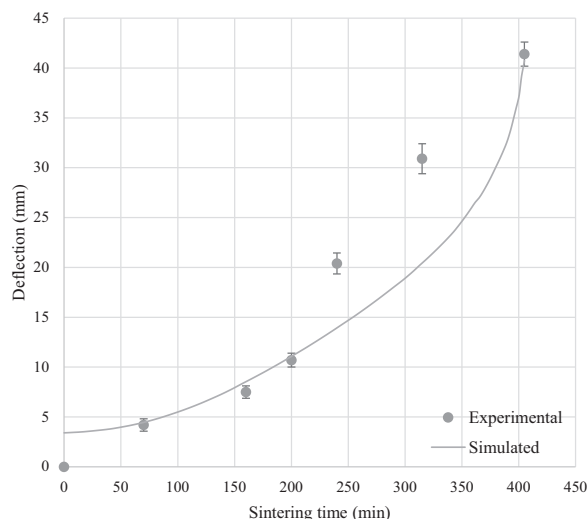
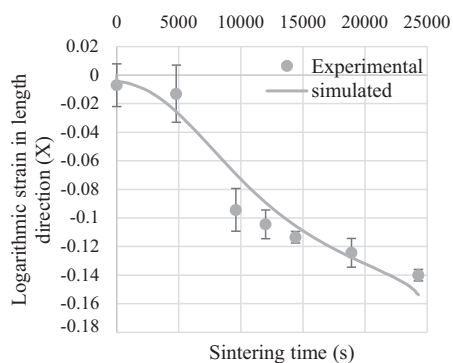
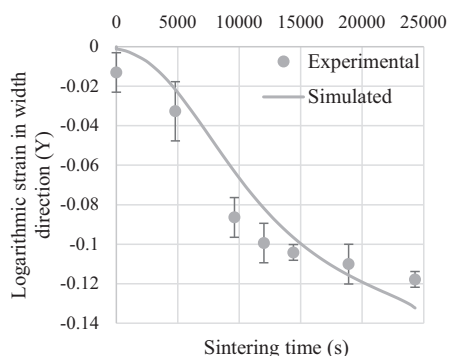


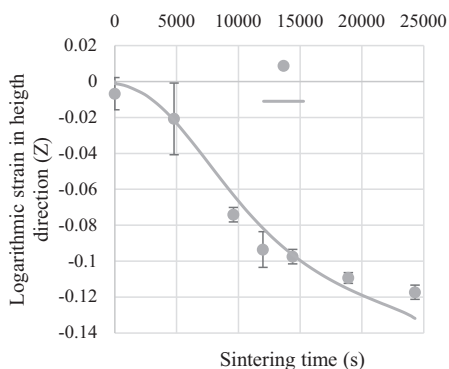
**Fig. 8:** Deflection of the midpoint deflection test obtained with finite element simulation.



(a)



(b)



(c)

**Fig. 9:** Comparison of linear shrinkage experimental data (PLC) with FE simulation during the sintering process in different directions (a) X-direction, (b) Y-direction, (c) Z-direction for midpoint deflection test.

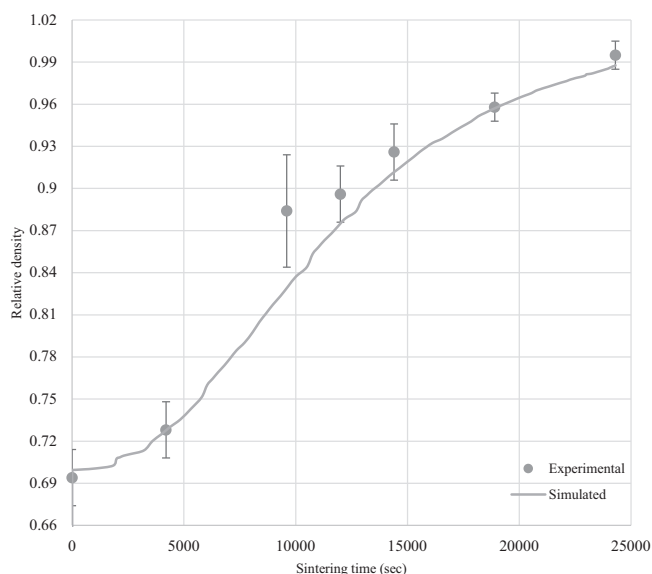


**Fig. 10:** Evolution of relative density during the liquid phase sintering process.

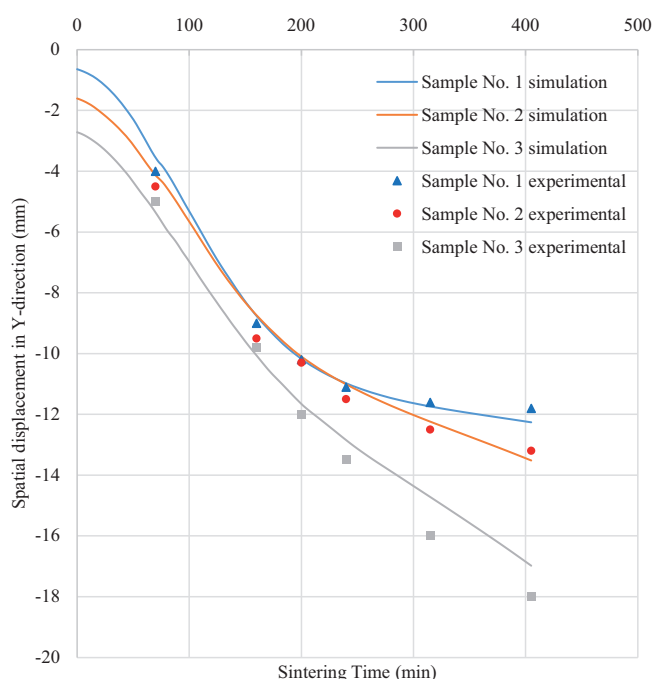


**Fig. 11:** Spatial displacement in Y-direction for sinter bending samples.

To validate the developed FE model in conjunction with the proposed model for the dynamic viscosity  $\eta$ , the deflection, spatial displacement in Y-direction, of the sinter bending samples is shown in Fig. 11 for both the model and experiment. It illustrates the relative good match between the model response and the experimental results. The maximum error is about 5 %. Moreover, this result shows that the sample with the greatest thickness exhibits significant resistance against deflection compared with the other samples. In other words, based on this hard porcelain composition, deflection may be suppressed by the increasing sample thickness.

To obtain more detail, the anisotropic shrinkage factor  $K_{xy}$  is plotted versus shrinkage along the X-direction in Fig. 12. It shows that  $K_{xy}$  is more extensive in midpoint deflection than in a free sintering test; in other words,  $K_{xy}$



in midpoint deflection test is far from the zero horizontal line in Fig. 12 in comparison with free sintering test. Therefore, the shrinkage anisotropy in the midpoint deflection sample is more critical than in the free sintering one.

Some important material properties obtained from the afore-mentioned validated sintering simulation are density distribution, effective shear and bulk viscosity, sintering and hydrostatic stress trend during the sintering process. As a first, the heterogeneous distribution of density for specimens in midpoint deflection and sinter bending test are shown in Fig. 13a and Fig. 13b, respectively. The relative density was distributed from 0.990 to 0.983 through the sample thickness, in the midpoint deflection test. In the sinter bending sample, the relative density was distributed non-uniformly around the contact area between sample and refractory support. Simultaneous influence of the gravitational and frictional force is mainly responsible for this heterogeneous density distribution. Besides, in the free sintering sample (Fig. 13c), the gravitational force brings neither inhomogeneous density nor deflection; however, the friction force hinders complete densification. In this case, the maximum density is reached uniformly to just 0.988.

The next simulation concerns the investigation of the rheological behavior of sample during the liquid phase sintering process. Fig. 14 shows the shear and bulk viscosity trend over the sintering time. Shear and bulk viscosity are responsible for resistance against deformation and volume shrinkage of the ceramic part during the liquid phase sintering process, respectively. From Fig. 14, the shear viscosity dropped suddenly from  $t = 0$  to  $t = 20000$ . This was

confirmed by the deformation of sample during this period of sintering time, which is due to vitreous phase formation and a decrease in its viscosity. This indicates that the shear viscosity is not stiff enough to offer sufficient resistance against the viscous flow deformation of the sample; however, the mullite growth strengthens the body against more viscous flow deformation and ends the falling trend of shear viscosity<sup>10, 28</sup>.

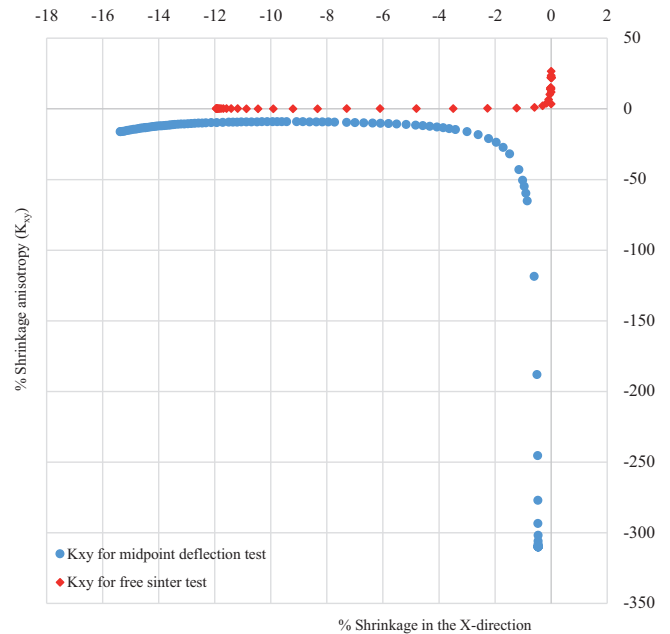


Fig. 12: Anisotropic shrinkage factor for midpoint deflection and free sintering test sample.

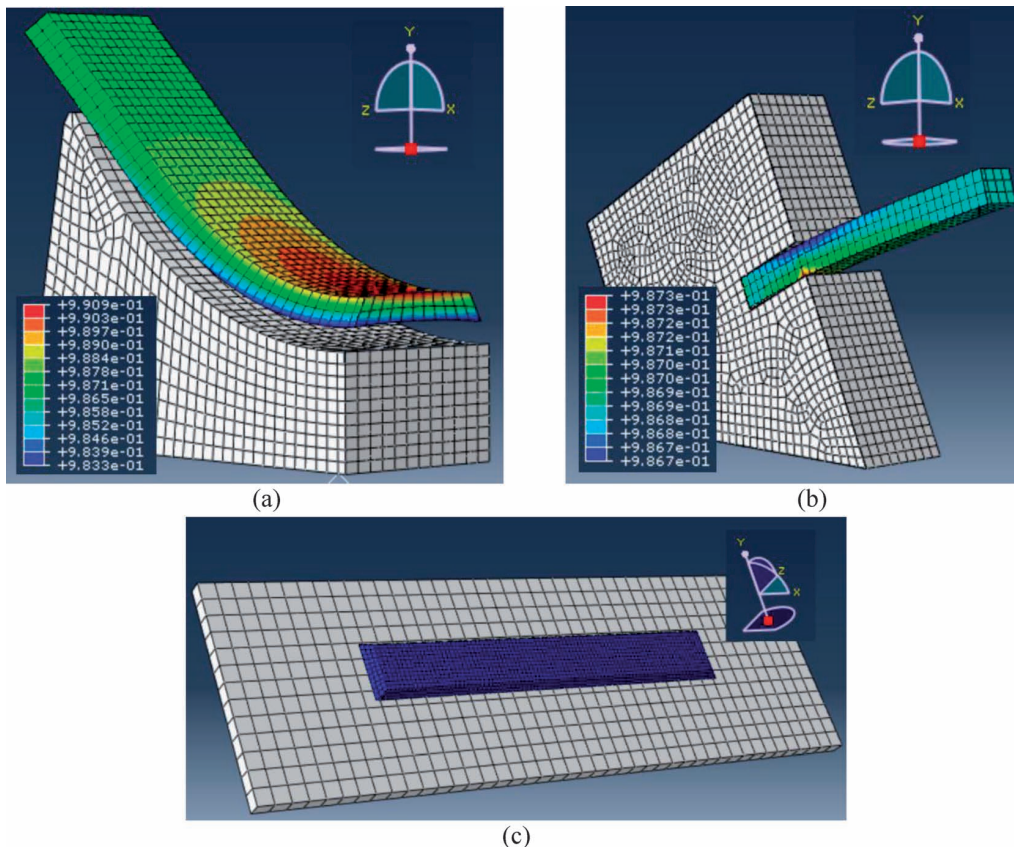


Fig. 13: (a) Heterogeneous densification after complete sintering process in midpoint deflection test; (b) non-uniform density distribution after complete sintering in sinter bending test set-up; (c) homogeneous densification after the free sintering test.

From Fig. 14, the bulk viscosity was reduced from  $t=0$  to  $t=10000$  s, then it rose in  $[10000, 24300]$  s. The decrease in the bulk viscosity may be related to the volume shrinkage of sample which started from  $t=0$  to  $t=10000$  s during the sintering process. The growth in the bulk viscosity may be attributed to the increased mullite content in the ceramic body during the final stage of the sintering process. It means that the sample resistance against volume shrinkage was increased by the bulk viscosity extension and secondary mullite growth, which is confirmed by the previous findings<sup>10,30</sup>. In addition, slight expansion at the final stage of sintering, in the mullite formation region (about 1200 to 1400 °C) has been proven by the dilatometry test result as shown in Fig. 15.

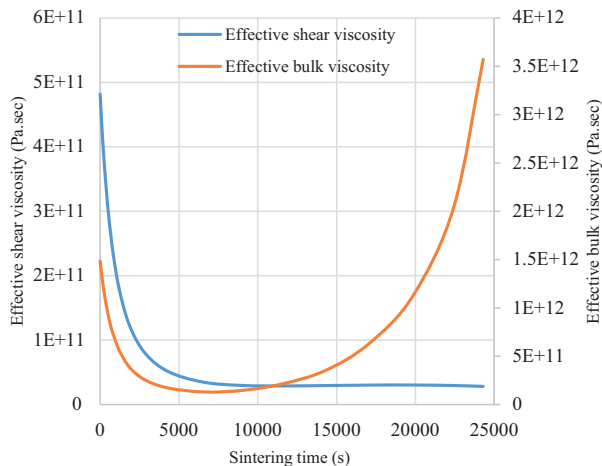


Fig. 14: Simulation of effective shear and bulk viscosity for the hard porcelain samples.

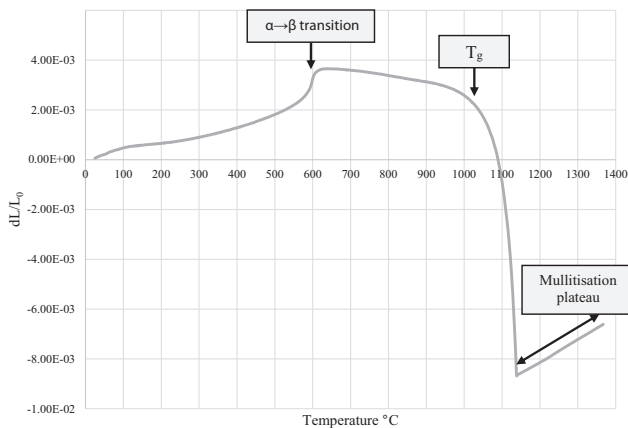


Fig. 15: Dilatometry test for hard porcelain sample from room temperature to about 1400 °C with a heating rate of about 21 K/min.

During heating in the dilatometry test, the body expands semi-linearly up to the quartz  $\alpha \rightarrow \beta$  transition, the effect of which has been recorded at 573 °C, then it continues to contract along a straight line to about  $T_g = 1000$  °C ( $T_g$ : glass transition temperature), it then shrinks abruptly from  $T_g$  to nearly 1150 °C, then very little expansion occurs owing to secondary mullite growth. This temperature range has been referred to in earlier studies as a “mullitization plateau”, that is a definite temperature interval in which the rate of shrinkage decreases and the shrinkage curve flattens<sup>10</sup>.

From the thermo-mechanical point of view, the sintering stress should be more than the hydrostatic stress during the entire sintering time until the sintering process has been completed. Therefore, according to Eq. 2, the green ceramic body will be sintered when the sintering stress ( $\sigma_s$ ) exceeds the hydrostatic stress ( $\sigma_m$ ). Sintering stress is the surface tension acting on the pore surface perpendicularly, and hydrostatic stress relates to internal pressure of entrapped air in each pore. As shown in Fig. 16, with increasing sintering time, more vitreous phase as well as a decrease in porosity content cause the sintering stress to increase; moreover, a decrease in the porosity diameter causes an increase in the hydrostatic stress. It is also concluded that the sintering stress remained higher than the hydrostatic stress during the entire sintering time.

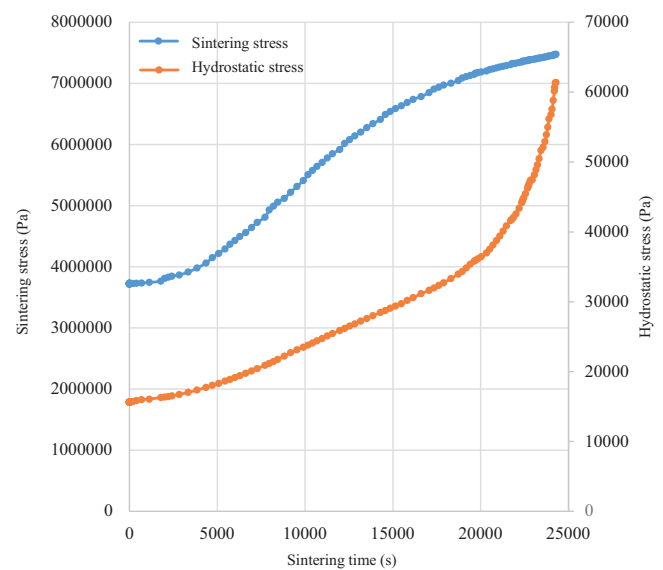


Fig. 16: Sintering stress and hydrostatic stress changing over sintering time.

SEM-EDX evaluations reveal that the porcelain sample has a heterogeneous microstructure after drying at 110 °C. It includes the broken solid materials and some porosity. Platelet shape of clay agglomerates, dispersed broken sharp edges of fine feldspar particles, as well as coarse quartz particles are obvious in the green porcelain body, as shown in Fig. 17.

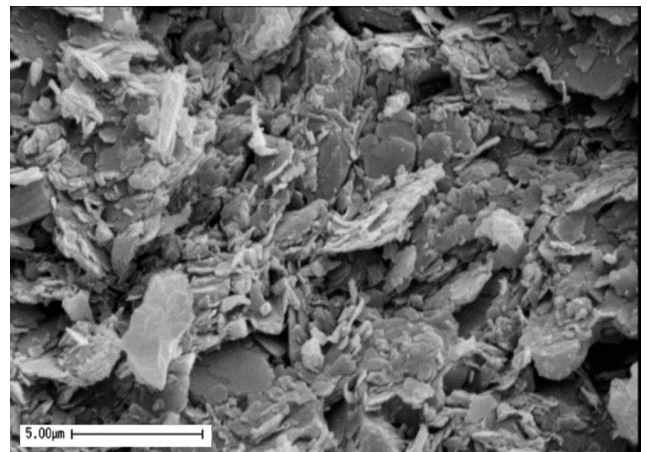


Fig. 17: Heterogeneous mixture of hard porcelain after drying at 110 °C.

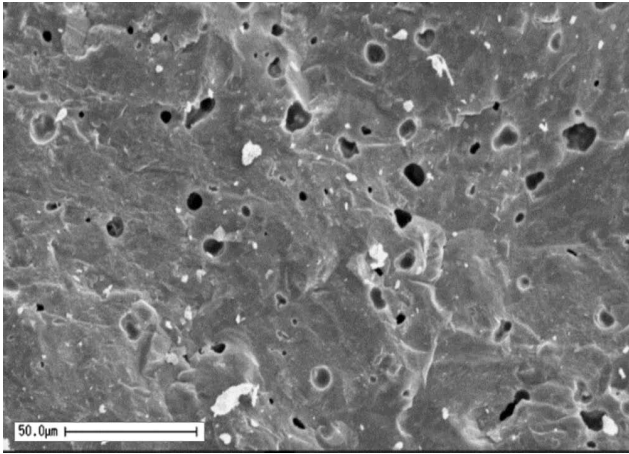


Fig. 18: Fully dense structure of hard porcelain after sintering at 1400 °C.

When the sintering temperature of about 1400 °C is reached, significant vitreous phase fills out the porosity, to produce a fully dense body. The morphology of the

porosity also became more spherical shape, as shown in Fig. 18.

After chemical etching of the polished sample surface, SEM-EDX investigations show the fine feldspar and quartz particles begin to melt and cause formation of a highly viscous liquid phase. The secondary mullite nucleus and colonies were enhanced from this liquid phase after sintering at 1200 °C (Fig. 19a). In addition, SEM-EDX evaluation shows the well-grown mullite crystals with high aspect ratio in the sample after sintering at 1400 °C (Fig. 19c). These needle-shaped long crystals formed three-dimensional interlocking networks, strengthen the porcelain and increase resistance against excessive pyroplastic deformation<sup>2, 10</sup>.

The XRD results show the phase evolution as a function of the increasing sintering temperature (Fig. 20). Kaolinite was detected as a major crystalline phase in the dried sample at 110 °C. Crystalline phases including quartz and feldspar were detected in all samples, from dried samples at 110 °C to sintered samples at 1200 °C. The low level of

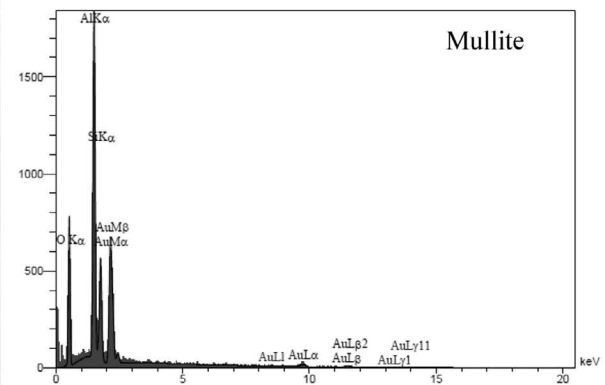
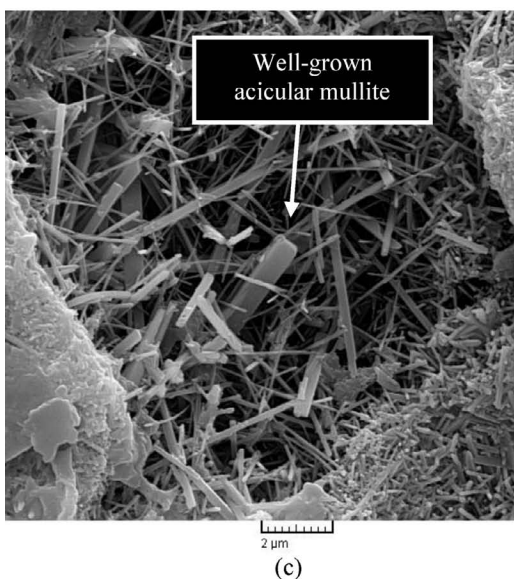
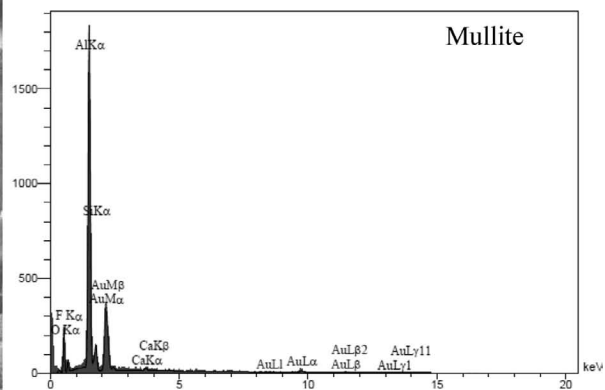
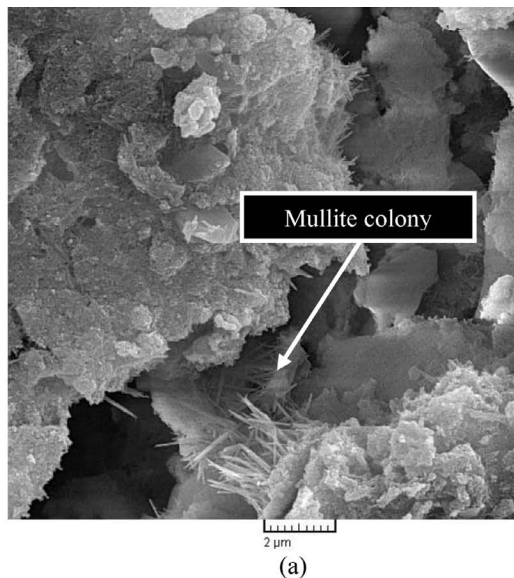


Fig. 19: (a) SEM for secondary mullite colonies, (b) EDX of mullite colonies after firing at 1200 °C, (c) SEM for mechanical interlocked acicular mullite, (d) EDX of well-grown acicular mullite after firing at 1400 °C.



glassy phase and secondary mullite crystals  $\text{Al}_2\text{O}_3 \cdot 2\text{SiO}_2$  in the sample fired at  $1200^\circ\text{C}$  in comparison with the higher amount of vitreous phase and mullite crystals in the sample sintered at  $1400^\circ\text{C}$  were determined by means of the MAUD method and baseline noises<sup>15,30–32</sup>. In addition, some residual quartz crystals were detected which remain insoluble in the vitreous phase in the sample sintered at  $1400^\circ\text{C}$ .

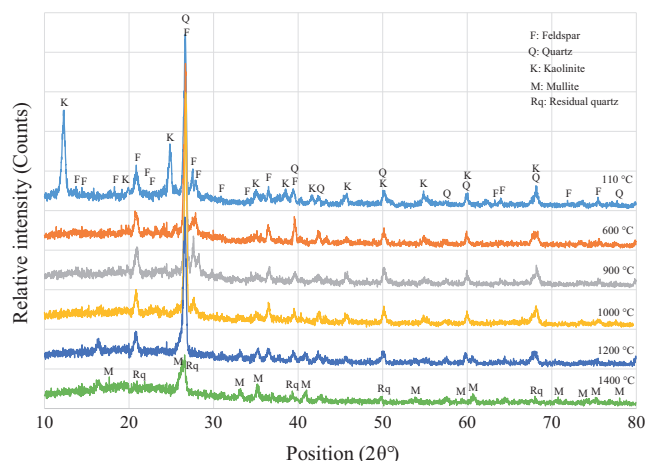


Fig. 20: XRD patterns of samples fired at different temperatures.

## VI. Conclusions

In this paper, pyroplastic deformation during liquid-phase sintering of a ceramic body was modeled with the finite element method. For this purpose, from some models to define the dynamic viscosity, which were obtained with the midpoint deflection test, the most suitable model was selected based on the Akaike information criterion. Outcomes of two experimental tests, namely sinter bending test and free sintering test, were used to validate the FE model. The results showed an excellent match between the experimental and the simulated outcomes. The validated model was utilized to predict certain physical, thermal, and rheological properties of the ceramic body including relative density, bulk and shear viscosity, sintering stress, and hydrostatic stress, which were confirmed in other experiments. Deflection outputs proved that the shear viscosity was well-defined with both dynamic viscosity and relative density. Densification and shrinkage results also confirmed that the bulk viscosity was well-defined with relative density. The sintering stress exceeded the hydrostatic process during the entire sintering process so the sintering process was completed. Dilatometry, SEM, XRD investigations as well as simulation results for bulk viscosity confirmed that the “mullitization plateau” was present as slight expansion at the final sintering stage. It is mainly attributed to the high amount of mullite formation. The pressure stress concentrates at the upper surface of the deflected sample, causing intensification of the densification process, whilst the tension stress on the mirror surface hinders the densification process. Heterogeneous density happens inevitably in both the midpoint deflection and sinter bending test. The anisotropic shrinkage factor  $K_{xy}$  implies that the shrinkage anisotropy in the midpoint deflection test happens during the liquid phase sintering process.

## References

- Blaine, D.C., German, R.M., Park, S.-J.: Computer modeling of distortion and densification during LPS of high-performance materials, Proceedings of the International Conference on Powder Metallurgy and Particulate Materials, Metal Powder Industries Federation, Princeton, NJ, 129–37, 2005.
- Gasik, M., Zhang, B.: A constitutive model and FE simulation for the sintering process of powder compacts, *Comp. Mater. Sci.*, **18**, 93–101, (2000).
- Molla, T.T., Bjørk, R., Olevsky, E.: Multi-scale modeling of shape distortion during sintering of bi-layers, *Comp. Mater. Sci.*, **88**, 28–36, (2014).
- Bene, P., Bardaro, D.: Numerical-experimental method to study the viscous behavior of ceramic materials, *J. Eur. Ceram. Soc.*, **34**, 2617–2622, (2014).
- Sarbandi, B.: Finite element simulation of ceramic deformation during sintering, Ph.D. thesis, Paris Institute of Technology, Mechanics of Materials, 4–10, 2014.
- Blaine, D., Chung, S.H., Park, S.J., Suri, P., German, R.M.: Finite element simulation of sintering shrinkage and distortion in large PIM parts, *PM Science and Technology Briefs*, **6**, [2], 13–18, (2004).
- Blaine, D.C., German, R.M.: Sintering simulation of PIM stainless steel, International Conference on the Powder Injection Molding of Metals, Ceramics, and Carbides, San Diego, CA, 2002.
- Mitsoulis, E.: Flows of viscoplastic Materials: modeling and computations, *Rheology Rev.*, 135–178, (2007).
- Andreev, D.V., Zakharov, A.I.: Ceramic item deformation during Firing: effects of composition and microstructure, *Refract. Ind. Ceram.*, **50**, [4], 45–52, (2009).
- Tuncel, D.Y., Ozel, E.: Evaluation of pyroplastic deformation in sanitary ware porcelain bodies, *Ceram. Int.*, **38**, 1399–1407, (2012).
- Bernardin, A.M., Souza de Medeiros, D., Riella, H.G.: Pyroplasticity in porcelain tiles, *Mater. Sci. Eng. A.*, **427**, 316–319, (2006).
- Dellert, A., Heunisch, A., Roosen, A.: The origin of anisotropic shrinkage in tape-cast green tapes, *Int. J. Appl. Ceram. Tec.*, **8**, 1312–1319, (2011).
- Sighinolfi, D.: Experimental study of deformations and state of tension in traditional ceramic materials, *Ceram. Mater.*, **63**, 226–232, (2011).
- Martina, S., Guessasma, M., Lechella, J., Adenota, F.: Simulation of sintering using a non-smooth discrete element method. application to the study of rearrangement, *Comp. Mater. Sci.*, **84**, 31–39, (2014).
- Blaine, D.C., Bollina, R., German, R.M.: Critical use of video-imaging to rationalize computer sintering simulation models, *Comput. Ind.*, **56**, 867–875, (2005).
- Olevsky, E.A.: Theory of Sintering: from discrete to continuum, *Mater. Sci. Eng.*, **R23**, 41–100, (1998).
- Arguello, J.G., Tikare, V., Garino, T.J., Braginsky, M.V.: Three-dimensional simulation of sintering using a continuum modeling approach, Sandia National Laboratories, Chapter 5, 2003.
- Olevsky, E.A., German, R.M.: Effect of gravity on dimensional change during sintering – part two. Shape distortion, *Acta Mater.*, **48**, 1167–1180, (2000).
- Shinagawa, K., Hirashima, Y.: A constitutive model for sintering of central powder compacts with internal structure due to granules, *Trans. Jpn. Soc. Mech. Eng.*, **64**, [617], 155–161, (1998).
- Shinagawa, K.: Internal stress diagrams of sintering stress versus viscosity for graded multilayers, *JSME Int. J. A*, **46**, [3], (2003).



- <sup>21</sup> Mohanram, A., Lee, S., Messing, G., Green, D.: A novel use of constrained sintering to determine the viscous Poisson's ratio of densifying materials, *Acta Mater.*, **53**, 2413–2418, (2005).
- <sup>22</sup> German, R.M., Chung, S-H., Blaine, D.: Distortion and densification control during liquid phase sintering of high-performance materials, Proceedings of 8<sup>th</sup> International Conference on Numerical Methods in Industrial Forming Processes, Columbus, OH, 2004.
- <sup>23</sup> Zuo, R., Aulbach, R., Rodel, J.: Experimental determination of sintering stresses and sintering viscosities, *Acta Mater.*, **51**, 4563–4574, (2003).
- <sup>24</sup> Theron, C.: Determination of sintering parameters for liquid phase sintering of silicon nitride, Ph.D. thesis, State University of New Jersey, 2008.
- <sup>25</sup> Tomandl, G., Varkoly, P.: Three-dimensional computer modeling of grain growth and pore shrinkage during sintering, *Mater. Chem. Phys.*, **67**, 12–16, (2001).
- <sup>26</sup> Shima, S., Oyane, M.: Plasticity theory for porous metals, *Int. J. Mech. Sci.*, **18**, 285–291, (1976).
- <sup>27</sup> De Jonghe, L.C., Rahman, M.N.: Sintering of ceramic, Handbook of Advanced Ceramics, Chapter 4, 2003.
- <sup>28</sup> Blaine, D.C., Bollina, R., German, R.M.: *In situ* characterization of apparent viscosity for continuum modeling of supersolidus liquid phase sintering, Proceedings of the 4<sup>th</sup> International Conference on Science, Technology and Applications of Sintering, Institute National Polytechnique de Grenoble, Grenoble, France, 307–310, 2005.
- <sup>29</sup> SIMULIA Dassault System, Abaqus user subroutines reference guide, section 1.1.1, pages 1–13, 2013.
- <sup>30</sup> Lee, S., Messing, G., Green, D.: Bending creep test to measure the viscosity of porous materials during sintering, *J. Am. Ceram. Soc.*, **86**, 877–882, (2003).
- <sup>31</sup> Porte, F., Brydson, R., Rand, B.: Creep viscosity of vitreous china, *J. Am. Ceram. Soc.*, **87**, 923–928, (2004).
- <sup>32</sup> Zanelli, C., Guarini, G., Raimondo, M., Dondi, M.: The vitreous phase of porcelain stoneware: Composition, evolution during sintering and physical properties, *J. Non-Cryst. Solids*, **357**, 3251–3260, (2011).
- <sup>33</sup> Cheng, B., Ngan, A.H.W.: The sintering and densification behavior of many copper nanoparticles: A molecular dynamics study, *Comp. Mater. Sci.*, **74**, 1–11, (2013).

